Heat-Generating Iron Oxide Nanocubes: Subtle "Destructurators" of the Tumoral Microenvironment

Jelena Kolosnjaj-Tabi,[†,‡] Riccardo Di Corato,[†,¶] Lénaic Lartigue,[†,§,¶] Iris Marangon,[†] Pablo Guardia,[∥] Amanda K. A. Silva,[†] Nathalie Luciani,[†] Olivier Clément,[‡] Patrice Flaud,[†] Jaykrishna V. Singh,[⊥] Paolo Decuzzi,[⊥] Teresa Pellegrino,[∥,#] Claire Wilhelm,[†] and Florence Gazeau[†,*]

[†]Laboratoire Matière et Systèmes Complexes, UMR 7057 CNRS/Université Paris Diderot, 10 rue Alice Domon et Léonie Duquet, F-75205 Paris Cedex 13, France, [‡]Inserm U970, Paris Cardiovascular Research Center-PARCC/Université Paris-Descartes, 56 rue Leblanc, 75015 Paris, France, [§]Laboratoire Matériaux et Phénomènes Quantiques, UMR 7162 CNRS/Université Paris Diderot, 10 rue Alice Domon et Léonie Duquet, F-75205 Paris Cedex 13, France, [∥]Nanochemistry, Istituto Italiano di Tecnologia, Via Morego 30, 16163 Genova, Italy, [⊥]Translational Imaging and Nanomedicine Departments, The Methodist Hospital Research Institute, 6670 Bertner Street, Houston, Texas 77030, United States, and [#]National Nanotechnology Laboratory of CNR-NANO, via per Arnesano km 5, 73100 Lecce, Italy. [¶]These authors contributed equally.

ABSTRACT Several studies propose nanoparticles for tumor treatment, yet little is known about the fate of nanoparticles and intimate interactions with the heterogeneous and ever-evolving tumor environment. The latter, rich in extracellular matrix, is responsible for poor penetration of therapeutics and represents a paramount issue in cancer therapy. Hence new strategies start aiming to modulate the neoplastic stroma. From this perspective, we assessed the efficacy of 19 nm PEG-coated iron oxide nanocubes with optimized magnetic properties to mediate mild tumor magnetic hyperthermia treatment. After injection of a low dose of nanocubes (700 μg of iron) into epidermoid carcinoma xenografts in mice, we monitored the effect of heating nanocubes on tumor environment. In comparison with the long-term fate after intravenous administration, we investigated spatiotemporal patterns of nanocube distribution, evaluated the evolution of cubes magnetic properties, and examined nanoparticle clearance and degradation processes. While inside tumors nanocubes retained their magnetic properties and heating capacity throughout the treatment due to a mainly interstitial extracellular location, the particles became inefficient heaters after cell internalization and transfer to spleen and liver. Our multiscale analysis reveals that collagen-rich tumor extracellular matrix confines the majority of nanocubes. However, nanocube-mediated hyperthermia has the potential to "destructure" this matrix and improve nanoparticle and drug penetration into neoplastic tissue. This study provides insight into dynamic interactions between nanoparticles and tumor components under physical stimulation and suggests that nanoparticle-mediated hyperthermia could be used to locally modify tumor stroma and thus improve drug penetration.

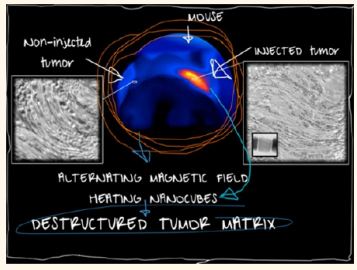

KEYWORDS: iron oxide nanoparticles · magnetic hyperthermia · cancer treatment · tumor microenvironment · extracellular matrix · collagen

Nanomedicines have raised new hopes for cancer treatment because of their promises to target more efficiently the tumor tissue and to deliver several therapeutic agents for combination therapy.[1] Among potential nanotherapeutics, metallic or magnetic nanoparticles also possess the unique ability to be activated on demand by external stimuli,[2,3] which could provide spatial and temporal control of therapy.[4] In the research for the most efficient agent for magnetic hyperthermia (HT), efforts have been focused on the design of nanoparticles, in order to improve their *intrinsic* properties and maximize their heating power by tuning their size, shape, magnetic material, or internal organization.[5−8] While iron oxide spherical nanoparticles were approved in EU as a medical device for magnetic tumor hyperthermia in brain[9,10] and prostate cancer,[11] in combination with radiotherapy or chemotherapy,[12−15] a more powerful alternative in terms of the specific loss power (SLP) has been recently proposed. The cubic nanocrystals turned to be more efficient nanoheaters than their spherical counterpart due to their diminished surface disorder and anisotropy.[6,7,16] Previously, we reported the synthesis and the water- and size-dependent heating performance of PEG-coated iron oxide magnetite nanocubes[6] and further demonstrated

* Address correspondence to florence.gazeau@univ-paris-diderot.fr.

Received for review October 14, 2013 and accepted April 16, 2014.

Published online April 16, 2014
10.1021/nn405356r

their biodegradability and biotransformation after injection in mice.[17] However, the potential of these biocompatible nanocubes was not yet evaluated *in vivo* for tumor treatment.

The penetration of therapeutics, including nanoparticles, throughout the tumor is still very challenging because of the strong heterogeneity of the tumor microenvironment and its disorganized vascular supply.[18] Like the majority of anticancer drugs, nanoparticles might not be able to access all tumor cells, resulting in some cells receiving a subtherapeutic exposure. Since the biomechanical dynamics of delivery in the tumor are complex and heterogeneous on the microscopic scale,[19] the mechanisms of distribution of therapeutics within tumors should be thoroughly investigated at relevant scales. Tumors consist of tumoral and stromal cells (such as endothelial cells, fibroblasts, and inflammatory cells), structural constituents of the extracellular matrix (ECM) (*i.e.*, collagen, elastin, proteoglycan, and glycosaminoglycan networks), and soluble components (like chemokines, growth factors, and cytokines), all of which are tightly related to neoplastic structure and progression.[20−23] In order to improve treatment effectiveness,[24] the development of anticancer nanoparticles has to focus as well on the effects of complex and poorly controlled interactions with the tumor stroma and on its role in the regulation of neoplastic evolution.[23,25] In this regard, nanotechnology may hold the promise to develop functional agents that are able to target and even to regulate the components of the tumor microenvironment.[24] The penetration, localization, and leakage of nanoparticles in the tumor depend on particles' size, shape, charge, and ligands, among other factors influencing particle interactions with the tumor components.[26−28] Primordial in providing structural integrity and angiogenic, mitogenic, and proteolytic factors, the peritumoral stroma also affects drug and nanoparticle penetration through enhanced interstitial fluid pressure, enhanced solid stress, chaotic vessel organization, and dense collagen barriers.[18,19,29] Recent strategies to improve nanoparticle penetration in tumors have focused on the vascular compartment and the passage across the vascular wall.[30−32] The physical activation of nanoparticles—producing heat or photosensitization—could be exploited to increase the vascular permeability and enhance the accumulation of nanosized (10−200 nm) agents within the tumor parenchyma.[33] However, the interstitial barriers, namely, the ECM, still hinder diffusion and convection of drugs and nanoparticles injected intravenously or intratumorally and must be overcome to achieve a homogeneous distribution of therapeutics close to tumor cells.[34] In the case of nanoparticle-induced hyperthermia, the spatial location of heating sources determines the temperature profile, which will differently affect tumor cells, depending on their localization with regard to nanoparticles. On the particle level, other mechanisms may come into play, as heat generation by nanoparticles under an alternating magnetic field (AMF) also depends on their local organization and environment. Several context-dependent factors, such as aggregation, cell internalization, and confinement or impaired mobility, can modify the nanoparticle response to the magnetic field and subsequently affect the conversion of the supplied magnetic energy into thermal losses.[35−37] Hence the heterogeneous and progressive structure of tumors should have radical consequences on the distribution, magnetic properties, and therapeutic efficiency of nanoparticles, through various mechanisms that are still to unravel. Conversely, the local heat generated by nanoparticles may also induce modifications of the tumor microenvironment. In our study, we sought to characterize the intimate spatiotemporal interactions of 19 nm PEG-coated iron oxide nanocubes[6] injected intratumorally, with the multiple players of the tumor environment. All over the treatment protocol (up to 3 cycles of magnetic field exposure), we combined a multiscale investigation of the nanoparticle distribution, biotransformation, and degradability (spanning the relevant scales from nanoscale to tissue and whole body levels). In addition, we characterized nanoparticles' magnetic behavior depending on their localization and evaluated their effects on the evolving tumor microenvironment. This study unveils the fate of (heating) nanocubes injected intratumorally and suggests that nanocube-mediated local hyperthermia has great potential not only to reduce tumor growth but also to modify the collagen-rich extracellular matrix and to facilitate the migration of nanoparticles and drugs (as exemplified by doxorubicin in the present study) through the tumor. In contrast, when nanocubes are cleared from the tumor to vital organs such as the liver and spleen, their magnetic potential is drastically reduced, preventing these organs from undesired heating.

RESULTS AND DISCUSSION

Tumor Hyperthermia and Tumor Growth. PEG-coated 19 nm nanocubes consisting of magnetite nanocubes stabilized in water by gallol-modified poly(ethylene glycol) molecules of 3000 MW, with optimized heating power,[6] were injected intratumorally into epidermoid carcinoma xenograft implanted in mice. The intratumoral administration (i.t.) is currently the only relevant route that can allow sufficient amount of localized nanoparticles to reach therapeutic temperatures (>42 °C) when submitted to AMF. Owing to the large specific loss power of 19 nm cubes (137 W/g in a magnetic field of 23.8 kA/m and frequency of 111 kHz), we injected a considerably lower dose (0.7 mg of iron) in comparison to previous studies in mice (25 mg for 10 nm spherical particles,[38] 7 mg for multicore nanoparticles,[39] or

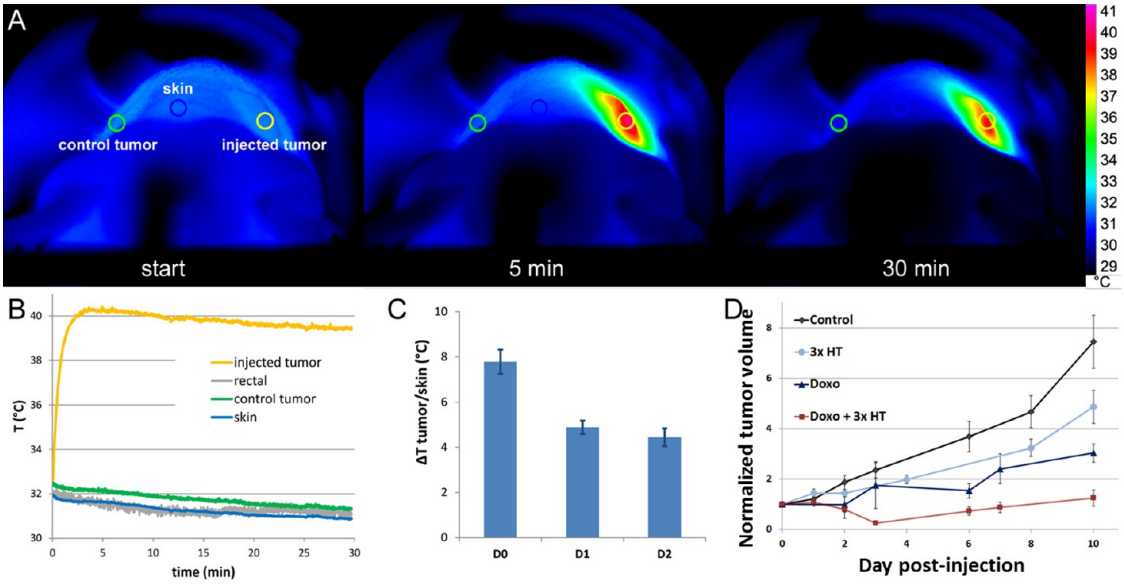

Figure 1. Nanocube-induced magnetic hyperthermia and its effect on the growth of solid tumors in mice. (A) Photographs taken by the thermographic infrared camera during the first AMF exposure (at the starting point, 5 and 30 min exposure time) of a mouse unilaterally injected in the right tumor with iron oxide nanocubes. The right scale represents the color code for surface temperature. (B) Graph of the temperature evolution over time during the first hyperthermia cycle under 30 min AMF exposure. The temperature was recorded either with the infrared camera (on injected and control tumor and skin on the neck) or with a fluoro-optic probe inserted in the rectum. (C) Temperature differences ΔT between the surface of injected tumors and the skin on mice necks, recorded on the day of injection (day 0, first AMF exposure) and day 1 and day 2 (second and third AMF exposure) after nanocube injection. Error bars represent the standard error of the mean (SEM) ($n = 16$). (D) Tumor growth curves of control noninjected mice (Control), mice injected with nanocubes and exposed to AMF on day 0, day 1, and day 2 (3× HT), mice injected intravenously with doxorubicin (Doxo), mice injected with doxorubicin (i.v.) and nanocubes (i.t.) and exposed to AMF (Doxo + 3× HT). Tumor volumes are normalized to the tumor volume on day 0 when the injection was made. Error bars represent SEM.

1−2 mg for bacterial magnetosomes).[40] In addition, we restricted the alternating field strength H and frequency f to maintain the product $H \times f$ below the critical limit of 5×10^9 A m^{-1} s^{-1}, for a clinically relevant, safe exposure to the ac magnetic field.[41] The animals were treated for up to three consecutive days by a 30 min AMF cycle per day, and the skin temperature of the mouse was monitored by a thermographic infrared camera (Figure 1A,B). The surface temperature of the injected tumor increased about 8 °C above the temperature of the skin on the neck, contralateral tumor, and rectal temperature (Figure 1A−C). For comparison, in the same volume and concentration fraction as the one injected into the tumors, the temperature of the nanocube suspension rose from 27 to 70 °C (Supporting Information Figure S1). When averaged over 16 distinct mice, the surface temperature of the injected tumor increased 7.8 ± 2.2 °C during the first HT cycle (day 0, 15 min postinjection) and 4.9 ± 1.2 °C and 4.5 ± 1.6 °C during the second and third AMF treatment at day 1 and day 2 postinjection, respectively (Figure 1C). Notably, the tumor growth was delayed by the three-cycle HT treatment (Figure 1D). To investigate whether AMF treatment could potentiate chemotherapy, tumors from AMF-treated and control animals were studied following intravenous injection of doxorubicin (6 mg/kg) (Figure 1D). The effect of doxorubicin alone on tumor growth was more important than the effect of the AMF treatment when chemotherapy was not concomitantly applied. Remarkably, the growth reduction was considerably enhanced when AMF hyperthermia and chemotherapy were combined.

Nanocube Distribution and Biotransformation at the Organism Level. The early distribution of nanocubes across the whole body of tumor-bearing mice was examined *in vivo* by MRI at day 6 after i.t. injection (Figure 2A). While a strong hyposignal was observed in injected tumor and in spleen (2-fold decrease in comparison to the controls), the liver, the contralateral tumor, and other organs including kidneys did not present any significant signal attenuation. Nanocube content was specifically quantified *ex vivo* by electron spin resonance (ESR) at day 10 postinjection in mice exposed to AMF or nonexposed mice. In contrast to elemental analyses that measure the total mass of iron—including endogeneous species—ESR exclusively quantifies the superparamagnetic/ferromagnetic nanoparticles, which present a well-characterized ESR spectrum at room temperature, with a sensitivity limit of 10^{-2} μg of iron.[42] Paramagnetic iron species, either endogenous or coming from the degradation of nanoparticles, are not quantified by ESR at 300 K since their signal is observed only at low temperatures (<50 K). At day 10 postinjection, the tumors injected with nanocubes still concentrated 30−40% of the nominal injected dose (0.7 mg), irrespectively of the treatment (Figure 2B), while a

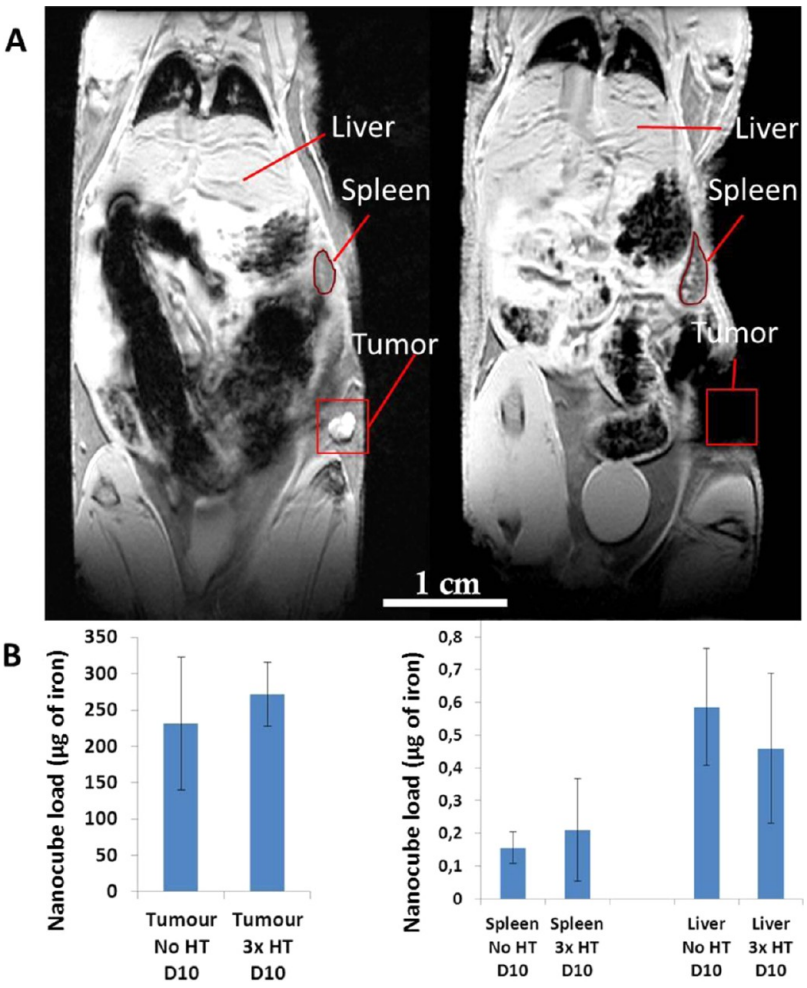

Figure 2. Follow-up of iron distribution in tumor-bearing mice *in vivo* and *post mortem*. (A) Comparison of MRI scans of a noninjected mouse (left) and a treated mouse intratumorally injected with nanocubes (right) taken *in vivo* at day 6 postinjection. A large hypointense signal, mainly localized in the tumor region denoted by a red square, is observed in the injected mouse. (B) Quantification of the nanocube load in tumor, liver and spleen by ESR. The nanocube load expressed in micrograms of iron was measured on dried organs 10 days after i.t. administration to mice that were either not exposed to AMF (no hyperthermia (no HT)) or exposed to three cycles of 30 min AMF exposure (3× HT). The mass of iron in the form of magnetic nanocubes, which show a characteristic ESR spectrum, is expressed as a mean ± SEM (n = 5 mice per condition).

fraction of the injected dose often leaked to the peritumoral subcutaneous or dorsal muscle tissue (Supporting Information Figure S2). ESR measurements also quantified the low percentage of cubes that could leak from the tumor to reach the spleen and liver (about 0.02 and 0.08% of the injected dose, respectively, corresponding to a concentration of 4×10^{-4} and 3×10^{-4} μg of iron per mg of organ) (Figure 2B), but did not detect any signal in contralateral tumors and kidneys. Such transfer of nanocubes is likely mediated by immune cells that could infiltrate the tumor before migrating to the reticulo-endothelial organs.

In order to monitor the nanocube fate and biodegradation processes in liver and spleen at longer time frames (over 4 months), we performed an additional study in which nanocubes were intravenously (i.v.) injected to healthy mice. The injected dose (50 μmol iron/kg, 56 μg per mouse) corresponds to the amount of iron that is conventionally used for clinical MRI. In comparison to noninjected mice, MRI monitoring showed a marked hyposignal in spleen and liver, which returned to normal over time, more rapidly in the liver compared to the spleen (Figure 3A). In line with *in vivo* MRI, where the signal decrease was 11-fold in the liver and 1.3-fold in the spleen, *ex vivo* ESR quantification showed that 30 and 2.5% of the injected dose (1.3×10^{-2} and 1.7×10^{-2} μg of iron per mg of organ) were found in the liver and spleen, respectively, 1 day after i.v. injection (Figure 3B). The nanocube concentration diminished to 2×10^{-3} and 7×10^{-3} μg/mg after 2 weeks and to 1×10^{-4} and 2.1×10^{-3} μg/mg after 4 months. It is worth noting that the residual nanocube concentration in liver and spleen 4 months after i.v. administration was still higher than the concentration that was transferred to these organs by immune cells following i.t. injection of a 12-fold higher dose. The strong decrease of nanocube concentration over time, which is faster in liver compared to the spleen, is the

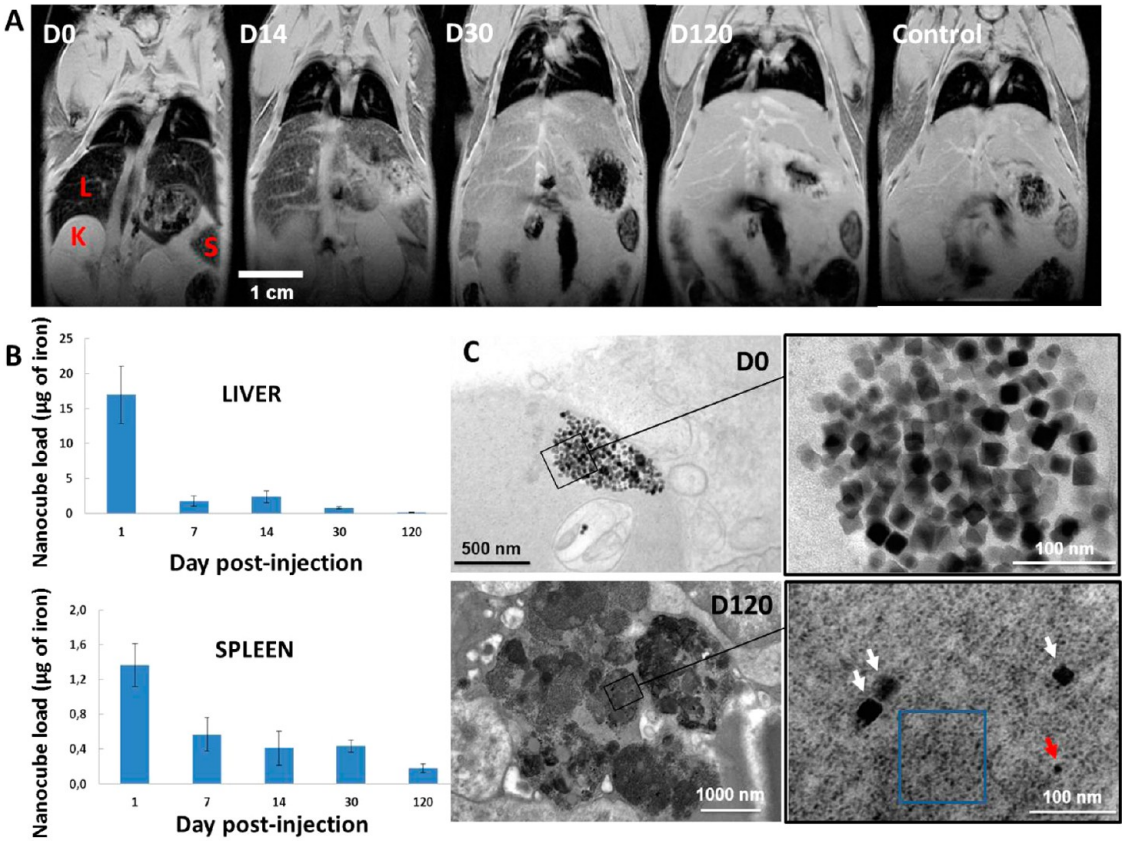

Figure 3. Follow-up of iron oxide nanocube clearance over a period of 4 months after intravenous injection in healthy mice. (A) Comparison of MRI scans of a control mouse and intravenously injected mice taken at D0, D14, D30, and D120 postinjection, showing a pronounced hypointense signal, mainly localized in the liver and spleen (letters L, S, and K denote the liver, spleen, and kidney, respectively) which is attenuating over time. (B) *Post mortem* quantification of nanocube load by ESR in liver and spleen over time. The mass of iron in the form of magnetic nanocubes is expressed as a mean ± SEM (n = 3 mice for each time point). (C) TEM micrographs showing a representative intracellular endosome loaded with nanocubes (left) and its magnified view (right), found in the spleen on the day of cube injection (D0, top); bottom micrographs show spleen sections harvested 4 months after injection: characteristic electron-dense lysosomes (right, and left for the magnified view) reveal the coexistence of scattered intact nanocubes (white arrows), a cube leftover (red arrow), and numerous monodisperse iron-rich ferritin proteins (blue square).

direct quantitative signature of the loss of nanocubes' superparamagnetic properties due to local biotransformation processes and transfer, as previously observed for iron oxide nanospheres.[42] In a previous work using high-resolution TEM, we revealed that PEG-coated nanocube crystals were individually degraded inside the lysosomes of spleen and liver macrophages, resulting in local iron release and transfer into ferritin, the iron storage protein.[17] Here the study was extended to 4 months, confirming the almost complete degradation of nanocubes and the ubiquitous presence of iron-rich ferritin proteins (Figure 3C). As previously shown for spherical 8 nm iron oxide nanoparticles, the resilient nanocubes and their nonmagnetic degradation products (*i.e.*, iron-rich ferritin proteins) are mainly accumulated in the spleen. Considering the kinetics of nanocubes degradation/elimination following i.v. administration, we can infer that such degradation could also occur in liver and spleen after i.t. administration: the very low nanocube content measured at day 10 may also result from their rapid biotransformation as suggested by TEM micrographs depicting conspicuous ferritin accumulation and degraded nanocubes in spleen (Figure 3C). In contrast, the nanocubes that are still remaining in the tumor (Supporting Information Figures S2 and S3) show almost no mark of degradation at day 10. Interestingly, their cubic shape remained globally intact, even after three-cycle HT treatment. This shows that the local heating of nanocubes did not induce melting and shape alterations that could affect heating power. Hence, the long persistence of intact nanocubes in injected tumors conjugated to the low transfer and high degradation rate within the spleen and liver seems favorable to an optimized efficiency of hyperthermia treatment in the tumor and little side effects in healthy tissues. These points are confirmed below through the evolution of the magnetic behavior of injected nanocubes.

Magnetic Behavior of Nanocubes in the Tumoral Environment. The magnetic properties of nanocubes were investigated in tumors at different time points over the treatment in order to follow the effects of nanocube

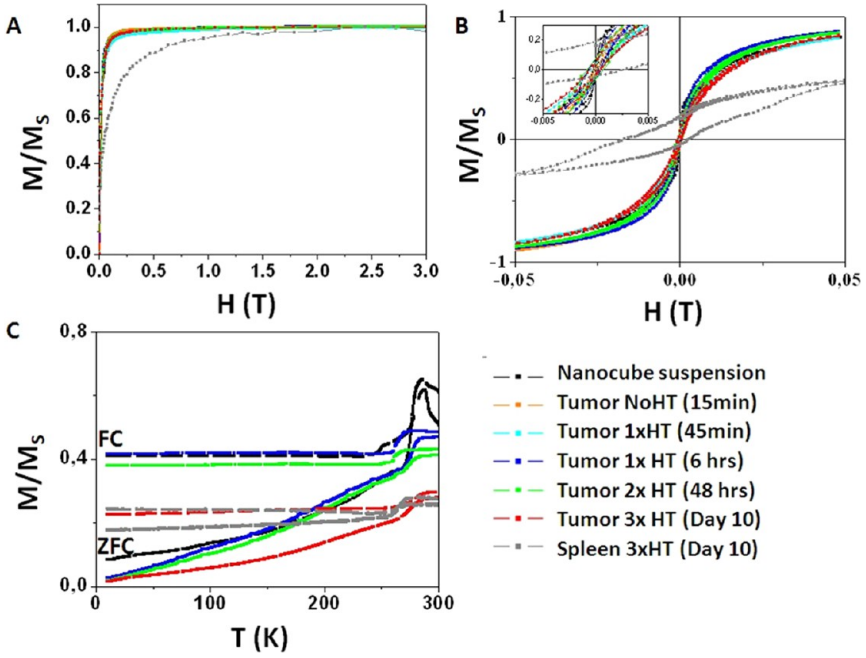

Figure 4. Kinetic characterization of nanocube magnetic behavior in tumor and spleen in comparison to the initial colloidal suspension. Magnetization measurements were performed in tumors at 15 min postinjection without AMF exposure (no HT), at 6 h postinjection following the first AMF exposure (1× HT), at day 1 following the second AMF exposure (2× HT), at day 10 after 3 AMF exposures (at day 0, day 1, and day 2), and in spleen at day 10 postadministration. (A) Field dependence of the magnetization *M* normalized to the saturation magnetization M_s (determined at 3 T) measured at 310 K. (B) Hysteresis cycle measured at 310 K in the magnetic field range of [−0.05, 0.05 T]. The inset shows a zoom over magnetic fields up to 5×10^{-3} T. Note the diminution of initial susceptibility over time in tumors and the drastic decrease of susceptibility together with increased hysteresis in spleen at day 10 postinjection. (C) FC and ZFC *versus* temperature in an applied magnetic field of 5×10^{-3} T. The field during sample cooling was also fixed to 5×10^{-3} T. Note the sharp increase in magnetization above 273 K due to retrieved mechanical mobility of the nanocubes in colloidal suspension and to a lesser extent in tumors at short time postinjection. The low field magnetization (normalized to the saturation value M_s) is strongly diminished at day 10 in spleen and in tumor. ZFC magnetization in spleen is closed to FC magnetization, reflecting frustrated state of nanocubes in intracellular compartments.

diffusion, immobilization, heating, cellular uptake, and eventual degradation: 15 min after i.t. injection without HT treatment, 6 h after injection following the first HT treatment, 48 h after injection following the second HT treatment, and 10 days postinjection after the three-cycle HT treatment. For comparison, the same magnetic measurements were performed in water suspension of nanocubes and in the spleen of tumor-injected mice at day 10. While the magnetization curves (normalized to the saturation magnetization M_s) in tumors were very close to that in colloidal suspension, the magnetization increased much slower with the magnetic field in spleen at day 10, indicating a partial deterioration of nanocube magnetic properties at this time in this organ (Figure 4A). The cubes in suspension did not show hysteresis at 310 K (Figure 4B), confirming that their magnetic moments follow the orientation of the magnetic field through Néel or Brownian mechanisms. The temperature-dependent field-cooled (FC)/zero-field-cooled (ZFC) magnetization further confirmed the superparamagnetic behavior of nanocubes at 310 K, with a maximum at a blocking temperature around 290 K. It must be noted that the sudden jump of magnetization at 273 K is due to the recovery of nanocube mobility upon thawing of the surrounding water (the cubes that did not undergo Néel relaxation below 273 K align along the field when they are free to rotate). Hence the amplitude of the magnetization jump at 273 K is indicative of the nanocube mobility in their local environment, while hysteresis in the magnetization curve measures the blockade of particle magnetic moment. Interestingly, the hysteresis curves were slightly open in tumors with a tendency to increase the coercive field and to decrease the initial susceptibility after 10 days. In line with these results, the Brownian jump was still observed but attenuated in tumors at day 1 and day 2 postinjection, suggesting partial mobility of intratumoral cubes. This mobility was impaired at day 10 in tumors, and the susceptibility was markedly degraded (M_{max}(50 G)/M_s = 0.24 *versus* 0.65 in colloidal suspension). In spleen, the coercive field was increased and the susceptibility decreased, which can be explained by the confinement and immobilization of nanocubes within intracellular lysosomes, which limit the rotation of individual magnetic moments. This is consistent with the hypothesis of a transfer of nanocubes from the tumor to the spleen by inflammatory macrophages. Such magnetic behavior on *ex vivo* tissues are consistent with *in vitro* results on cultured cells (data not shown) showing that cell internalization

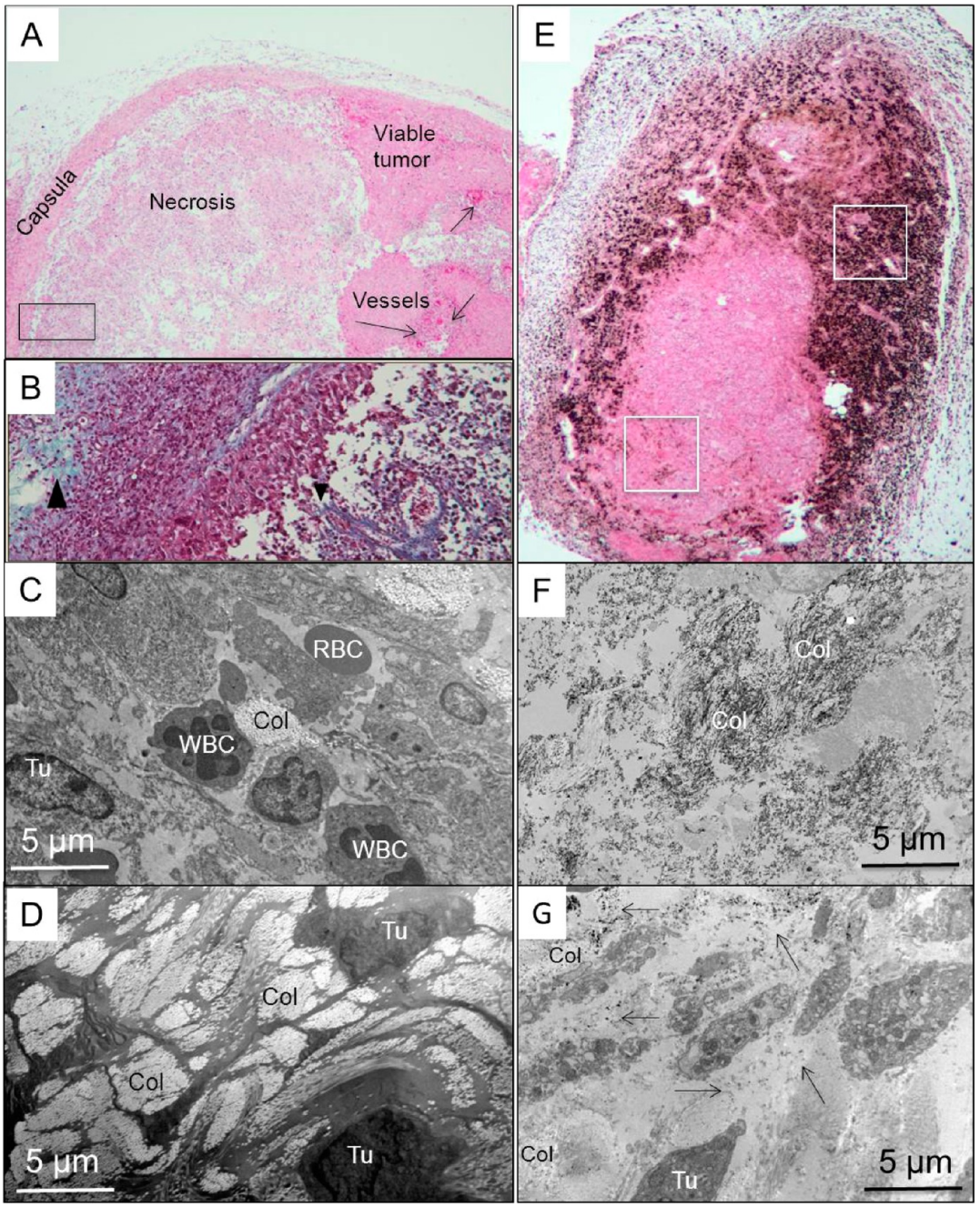

Figure 5. Microstructure of control (A–D) and nanocube-injected (E–G) tumors at day 1 postinjection. (A) Hematoxylin–eosin (HE) staining of histological sections showing the typical control tumor structure, which includes the capsula surrounding the tumor, the zones of cell necrosis where cells exhibit diminished cohesion and immune cell infiltration, and the zones of viable, vascularized tumor tissue (4× magnification). (B) Histological micrograph of the same tumor after Masson trichrome staining, showing the characteristic turquoise staining of collagen fibers, abundantly present in the tumor capsula (large arrowhead) and infiltrating the tumor stroma as a mesh-like structure (small arrowhead) (20× magnification). (C) TEM micrograph showing a typical necrotic zone, including tumor cells (Tu), infiltrating white blood cells (WBC), extravascular red blood cells (RBC), and collagen bundles (Col). (D) TEM micrograph showing the structure of collagen-rich tumor capsula with disseminated cohesive tumor cells. (E) Optical micrograph of a nanocube-injected tumor after HE staining, showing the intratumoral distribution of injected nanoparticles (brown color), which are dense in the pericapsular zone and more scattered in the tumor core. (F,G) TEM micrographs showing the mainly extracellular nanocube distribution in the collagen-rich capsula zone, outside and between the collagen fibers (F) and in the tumor core (G), located among surrounding collagen fibers (arrows).

decreases susceptibility, impairs the mobility of nanocubes and diminishes their heating power.[43] It is worth noting that the magnetic behavior of nanocubes in tumors lies between their behavior in water (mobile nanocubes without hysteresis) and that found in spleen after macrophage internalization and partial degradation. This macroscopic outcome is consistent with micro- and nanoscale observations of cubes in tumors (Figures 5 and 6), showing intact cubes mostly in the extracellular matrix, while all the cubes in spleen or liver

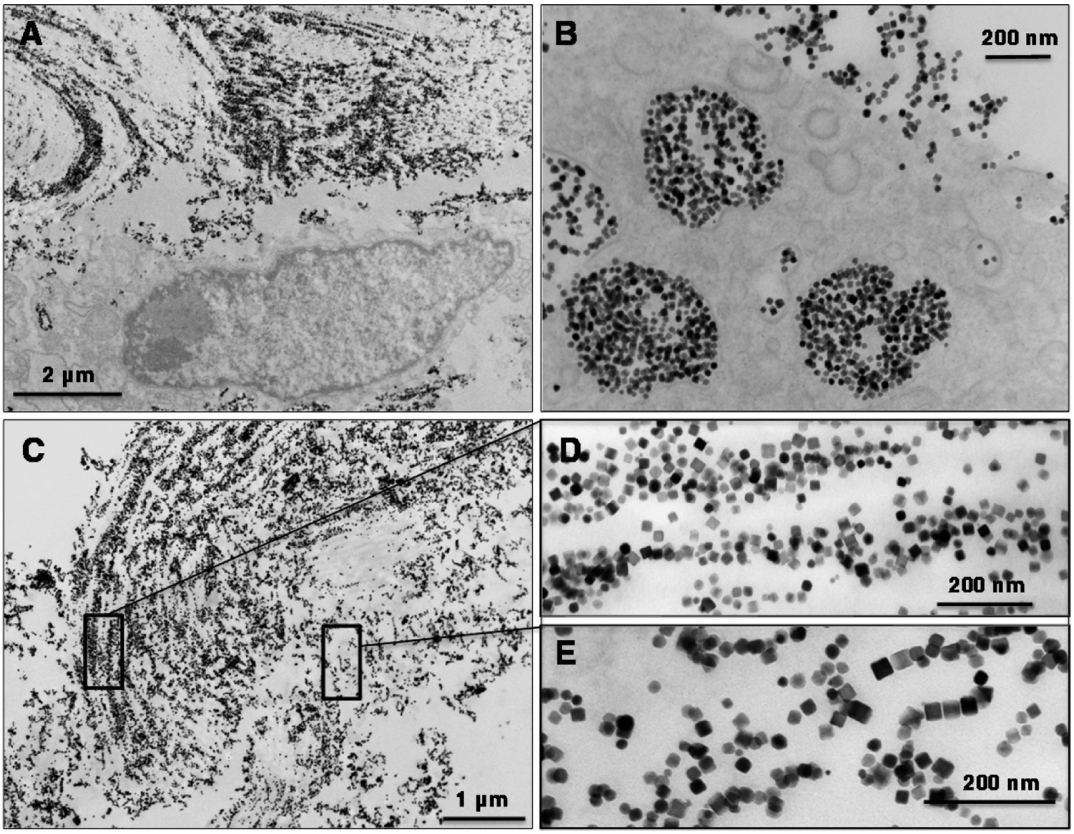

Figure 6. TEM micrographs showing intratumoral distribution of nanocubes 15 min after i.t. injection. Nanocubes are mainly located in the extracellular matrix (A), despite the fact that a minor fraction of cubes are internalized by cells and confined in cell endosomes (B). In the extracellular matrix (C), the nanocubes are distributed between the collagen fibers, following the highly structured collagen organization (D) or in collagen surroundings where the cubes freely form chains or aggregates (E).

had intracellular lysosomal location (Figure 3C). Hence extracellular nanocubes are still mobile in tumors in the first days postinjection, but the increasing cellular uptake by tumor and stromal cells progressively diminishes their magnetization and slows down their dynamics. Such observations on the magnetic behavior of nanoparticles have two important consequences regarding hyperthermia treatment. First, the original magnetic properties of the nanocubes are almost unspoiled once the particles are in the tumor (at least the first days following injection and HT treatments) due to their predominantly extracellular localization and good dispersibility. This should ensure that the nanocubes would present heating properties that are close to that of the colloidal suspension, in which their SLP has been optimized by tuning the particle's shape and size.[6] This allows repeating the treatment without substantial loss of the heating efficiency, although the temperature increments diminish with time (Figure 1C), probably due to partial cell internalization, nanocube clearance, and redistribution in the tumor as we will detail later. The second critical result is that the nanoparticles that were cleared from the tumor to other organs (*e.g.*, spleen and liver) show strongly deteriorated magnetic properties, due to cell internalization, confinement, and the onset of degradation. Hence, irrespective of their local intracellular concentration, their decreased magnetization (at the field strength of AMF treatment) would prevent substantial heating and save the reticulo-endothelial organs from heat-induced side effects.

Local Distribution of Nanoheaters and Hyperthermia Effects on the Tumor Microenvironment. After intratumoral injection, the local distribution of nanocubes was the result of complex interactions with the tumor microenvironment. Histological and TEM examination of epidermoid tumors, prior the injection of nanoparticles, shows a typical structure that resembles human tumors consisting of a collagen-rich capsula, delimiting the tumor mass, and a tumor core with scattered necrotic areas and neoplastic nodules that comprise vessels (Figure 5A). Masson trichrome staining (Figure 5B) reveals that collagen (stained in turquoise) is not only prominent in the tumor capsula or between the nodules but it also infiltrates the tumor core region with a mesh-like lattice. The TEM confirmed the highly organized fiber structures of collagen in the tumor interstitium, which form large bundles between stromal and tumor cells (Figure 5C,D). The same structural features were observed soon after nanocube injection (Figure 5E). Remarkably, the nanocube distribution (in brown on H&E staining) mainly follows the collagen distribution (Supporting Information Figure S4), being very concentrated around the

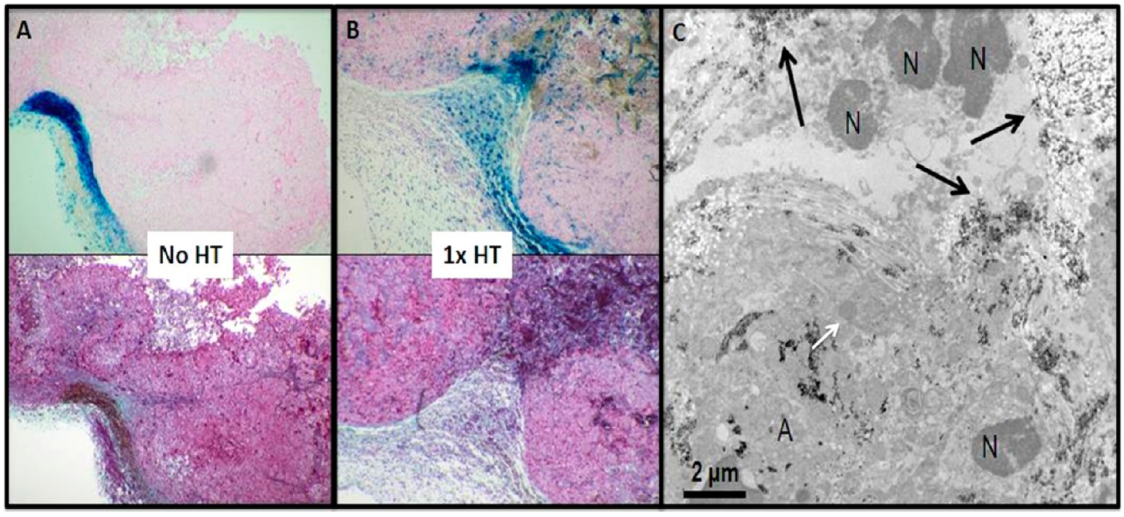

Figure 7. Inceptive effects of magnetic hyperthermia. (A) Histological micrograph showing particle distribution in a tumor that was injected with iron oxide nanocubes but not exposed to AMF. The peripheral and compact nanocube-rich region is revealed in blue after Pearls staining (top panel) in close proximity to the compact collagen fibers revealed in turquoise by trichrome staining (bottom panel; nanoparticles are seen in brown). (B) Histological micrograph of a tumor after AMF exposure treatment show scattered nanocube aggregates invading the tumor core (blue spots after Pearls staining, top panel) and slackened collagen fibers on trichrome staining (bottom panel). (C) TEM micrographs of treated tumors show dying cells with condensed nuclei. *N* denotes nucleus of necrotic cells. *A* labels fragments of an apoptotic cell (the white arrow is pointing at an apoptotic body).

tumor in the capsula and more diffuse and mesh-like when approaching the core (Figure 5E). Moreover TEM observations demonstrate elongated and curved organizations of nanocubes that tightly follow the long fiber structures of collagen in the capsula (Figure 5F and Supporting Information Figure S5). In cell-rich regions of the tumor core (Figure 5G), the nanocubes are less densely distributed and are found mainly in the interstitial free space and in collagen bundles and more rarely within cells (Figure 6A,B), where particles are found close to cellular membranes and occasionally internalized in cell endosomes and lysosomes. Note that the nanoscale organization of cubes (isolated, as chains or as large isotropic aggregates) depends on the local interactions with fibers of the extracellular matrix (Figure 6C−E).

Conversely, already after the first hyperthermia cycle, optical microscopy clearly indicated that both nanocubes and collagen fibers, which generally colocalized and looked compact in nonheated tumors (Figure 7A and Supporting Information Figures S5), started to diffuse and slacken (Figure 7B). As exemplified in Figure 7B, the nanocubes penetrate more deeply in the cell-rich tumor core after HT, while the collagen structures become looser. After HTs, we could observe large necrotic areas by optical microscopy (Figure 7B and Supporting Information Figure S6), while TEM examination revealed both necrotic and apoptotic cells in the vicinity of nanoparticles (Figure 7C). In order to quantitatively confirm that AMF exposure has the ability to change the collagen fibril organization, we have measured the mean interfibrillar distance in the collagen bundles of control tumors without injection of nanocubes (Figure 8A), after injection of nanocubes, without hyperthermia (Figure 8B), and after the first AMF exposure (one HT treatment) (Figure 8C). We found statistically significant changes in the interfibrillar space, which increased from 101 ± 17 nm in controls to 133 ± 32 nm in injected tumors after AMF exposure (p = 0.0112). In contrast, there was no statistically significant difference between controls and nonexposed injected tumors, which had the interfibrillar spacing of 97 ± 34 nm (Figure 8D).

Following the observed spatial distribution of nanocubes, presenting a massive accumulation within the collagen-rich capsula delimiting the tumor mass (Figure 5A), a finite element model was built to predict the spatiotemporal distribution of the temperature field $T(\mathbf{x},t)$ within the tumor and the surrounding tissues (see supplementary S7 for details).[44,45] As depicted in Figure S7, the geometry of the model comprises an inner tumor region (Ω_3), depleted of nanocubes; a capsula (Ω_2) surrounding the tumor core, where most nanocubes are deposited; and the healthy tissue (Ω_1), which is in direct contact with air, on the skin side, kept at 25 °C and the rest of the animal, kept at 31 °C. Upon exposure to AMF, heat is generated by the nanocubes only in Ω_2 and distributed to the surrounding domains over time. At steady state, a maximum temperature of ∼39 °C is reached within the collagen-rich capsula and the skin of the animal, in very good agreement with the experimental observations documented in Figure 1. The tumor core, Ω_3, which is completely surrounded by the capsula, reaches a slightly lower temperature of ∼37 °C (310 K). This is ∼6 °C higher than the normal animal temperature (∼31 °C) under anesthesia and could induce thermal damage on tumor cells observed

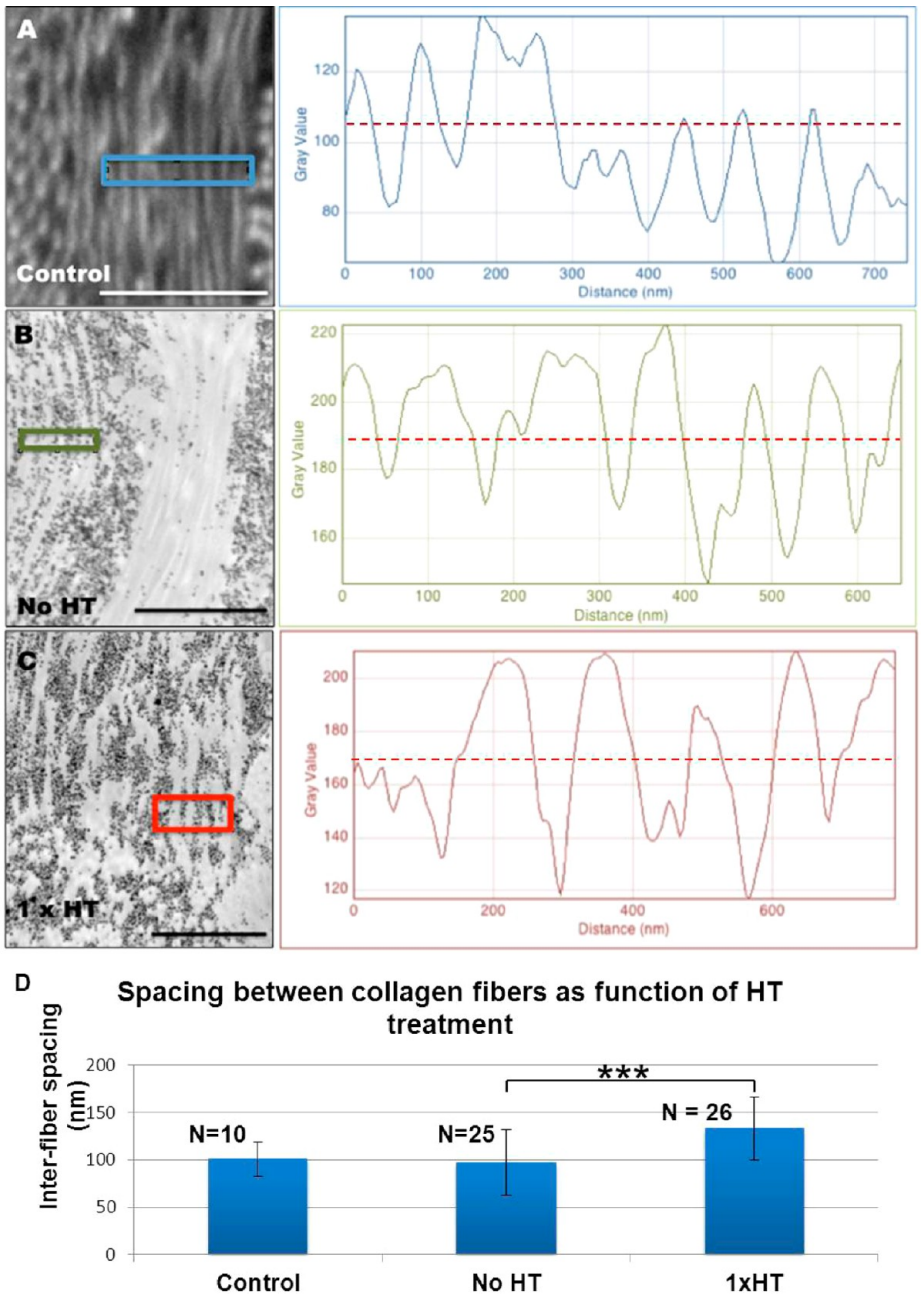

Figure 8. TEM micrographs of the collagen-rich extracellular matrix in control tumor (A), injected tumor that was not exposed to AMF (B), and injected tumor after the first 30 min AMF exposure (C), with respective examples of interspacing measurements (gray stripes) between collagen fibers (white stripes or dots, when cut in the axial direction). Curve maxima that have a gray intensity value above the dashed line are counted as interfibrillar spacing. When nanocubes diffuse between the fibers, there is a shift toward higher gray values. Scale bars in TEM micrographs correspond to 1 μm. (D) Mean interfiber spacing of intratumoral collagen fibers measured under each condition. The error bars represent the standard deviation. All error bars reflect SD (n = 3); * indicates $p < 0.001$ of injected and AMF-exposed tumors *versus* injected and not exposed tumors.**

on histology and TEM images (Figures S6 and 7C), with subsequent effect of reduced tumor growth.

Nanoparticle-Mediated Hyperthermia Induces Phase Transitions in Collagen Networks *in Vitro* and Improves Nanoparticle Penetration. In order to confirm the outcome of nanocube-mediated hyperthermia on collagen structures, we performed additional experiments on collagen gels reconstructed *in vitro* (see supplementary S8 for a detailed description). We first assessed the diffusion of nanocubes into the collagen structure by depositing a drop of nanocube suspension at the top of the three-dimensional collagen gel. Similar to the observations in tumors, the front of nanocube diffusion was moving ahead into the collagen gel when the alternating magnetic field was applied (Figure S8A). This finding suggests a phase transition of the collagen network in contact with heating nanocubes that lets the cubes penetrate in depth depending on exposure time.

In a second series of experiments, we studied thermal phase transitions in collagen hydrogels incorporating increasing concentrations of nanocubes (Figure S8B). In contrast to the nanocubes dispersed in water which heat monotonously toward the equilibrium plateau (Figure S1), the heating curves of nanocube-loaded collagen gels present an intermediate plateau, suggesting endothermic transition. This behavior may be ascribed to thermally induced destabilization of the collagen hierarchical structure as previously observed by differential scanning calorimetry.[46,47] This hypothesis is also supported by TEM observations of the collagen gels before and after AMF exposure: the collagen fibrils in close contact or in the proximity of nanocubes show severe structural modifications after AMF treatment (Figure S8D). Nanocube heating may induce defibrillation of adjacent proteins, whereas more distal fibrils remain intact. Therefore, phase transition of the collagen might occur locally depending on the spatial distribution of nanocubes. Overall, this *in vitro* study corroborates our *in vivo* findings that the interstitial collagen-rich matrix can be modified by local hyperthermia, leading to phase transitions, destabilization of collagen bundles, defibrillation, and subsequent enhanced penetration of nanoparticles.

Nanoparticle-Mediated Hyperthermia: A Local and Temporally Controlled Treatment To Modify the Extracellular Matrix. Our multiscale monitoring of 19 nm nanocubes injected intratumorally leads to the conclusion that the tumor environment essentially determines the nanocube distribution and their response to AMF exposure. Our first striking result is that the collagen network functions as a sink for most of the cubes. This is in line with previous studies suggesting that collagen fibers significantly contribute to interstitial resistance due to their nonisotropic orientation and high surface area.[18,48] Electrostatic interactions with charged components of the interstitial space (slightly positive for collagen fibers and highly negative for glycosaminoglycan or hyaluronan) also influence the transport of charged nanoparticles.[18] Hence the mobility of nanoparticles should result from the interplay between steric, hydrodynamic, and electrostatic interactions. If small therapeutic agents of a few nanometers and flexible macromolecules can efficiently diffuse in the tumor interstitial matrix, particles that exceed the size of 10 nm start being restrained by interfibrillar spacing, and liposomes or viruses larger than 60 nm are not able to penetrate along the interstitial space.[49] Here the 19 nm PEG-coated nanocubes injected intratumorally are found concentrated along and within collagen fibers, underlining the highly heterogeneous and anisotropic microstructures of the extracellular matrix. Therefore, the pattern of collagen distribution mainly determines the nanocube transport and propagation from the injection point. Remarkably, the nanocube distribution appears to discriminate different phases of the matrix. The aqueous phase, characterized by a low fiber concentration (and high available volume fraction), low polysaccharide content, and low viscosity, contains a large density of mobile nanocubes that frequently assemble as chains or form fractal structures (Figure 6E). In contrast, highly organized fibrous collagen restricts the nanocube diffusion to the unidirectional interfibrillar aqueous space (Figures 6D and 8 and Figure S5). This multiphase distribution of nanocubes may reflect the interactions and transport ability of PEG-coated cubes in the different phases of extracellular matrix.[34,50] While multicore particles with negatively charged carboxymethyl dextran coating show aggregation, immobilization, and massive cellular uptake in tumor environment,[39] we hypothesize that the neutral, hydrophilic, and molecular structure of PEG coating accounts for the high dispersibility and interstitial localization of our cubes.

Not only the collagen content but also the organization of its fibrillar network vary with the tumor type and location and differently affect the distribution of both i.t. and i.v. injected nanotherapeutics.[49] In our model of epidermal carcinoma A431 xenograft, tumors show a thick fibrous capsula from which septa spread into the tumor stroma, giving the tumor mass a lobulated pattern (Supporting Information Figure S9) and a mesh-like collagen structure in the vicinity of tumor and immune cells. Interestingly, the nanocubes are able to distribute in both the capsula and the mesh-like network to partially penetrate the tumor parenchyma close to neoplastic cells, provoking thermal damages and tumor cell apoptosis (Supporting Information Figures S6 and S10). However, in contrast to dextran-coated 45 nm nanoparticles that show rapid cell internalization in a breast adenocarcinoma xenograft,[51] only a minor fraction of the PEG-coated nanocubes were found within intracellular compartments of tumor cells and the heat generation mainly occurred in the extracellular space, in which nanocubes keep their original magnetic properties and heating efficiency. Conversely, the nanocubes that migrated to distal tissues lose their heating potential due to endosome confinement and ongoing biodegradation. While intracellular confinement, degradability, and biotransformation of nanocubes warrant the long-term safety of the treatment, its therapeutic efficiency relies on midterm extracellular and intramatrical persistence of nanocubes.

Apart from the individual capability of nanoheaters, the heating pattern within the tumor mostly depends on the heterogeneous penetration of nanocubes at the tissue level. Here the most striking effect of the hyperthermia treatment is an apparent redistribution of the nanocubes within the tumor. While higher vascular permeability, decrease in diffusion resistance (due to the death of cancer cells in some tumor regions), and increase in local pressure[38,52,53] may

influence the distribution of nanoparticles, our experimental evidence reveals that nanoparticle-mediated hyperthermia also affects the morphology, interfibrillar space, and organization of intratumoral collagen fibers. This is further confirmed by *in vitro* experiments on biomimetic type I collagen networks showing phase transition of collagen, local denaturation, and subsequent penetration of nanocubes, induced by AMF treatment. Since extracellular acidity is more prominent in tumoral tissue,[54] it is noteworthy that the type I collagen[49] exhibits a double thermal transition in the acidic solution.[47,55,56] A minor reversible thermal transition within 31−37 °C arises from the depolymerization of the smallest collagen fibrils, whereas the major irreversible thermal transition occurs in the 37−55 °C temperature range, due to total defibrillation and unfolding of the native triple helical structure of collagen.[47] Interestingly, some studies suggested that the efficacy of hyperthermia might depend on the lower extracellular pH of tumors,[57,58] which can be related to the fact that decreasing pH decreases the transition temperature of collagen fibers.[59] Recently, different strategies have been proposed to destructure the extracellular matrix and permeate the extracellular compartments more freely. The degradation of fibrillar collagen with bacterial collagenases,[60] antifibrotic agent,[49] or matrix metalloproteinases[61,62] has been shown to increase the transport of oncolytic viruses or doxorubicin-loaded liposomes delivered both intratumorally and intravenously. However, the systemic injection of matrix modifiers may also induce toxicity for normal tissues or stimulate the migration of cancer cells out of the primary tumor.[63] Therefore, as the ECM is known to have a rapid rate of turnover, a gentle, local, and time-controlled treatment using magnetically induced hyperthermia could have decisive advantages. In contrast to soluble matrix modifiers, heat-induced ECM destructuration is reduced to the zone of accumulation of nanoheaters, thereby eliminating adverse effect on healthy tissues. Furthermore, the nanoheaters can be activated on demand by external magnetic field at any time of the treatment. The intratumoral persistence of nanoparticles with preserved heating capacity gives the opportunity for repeated AMF exposure as exemplified in our study. The first treatment serves to modify the local fibrillar environment of nanoparticles and favors their progression from the capsula to the tumor bed and from the mesh-like collagen structure of the tumor core close to tumor cells. The second and subsequent HT exposures affect a larger area of the tumor and induce thermal injuries to stromal and tumor cells, which reduce tumor progression as observed in our study. Noticeably, heat-induced degradation of the collagen hierarchical network would also have the potential to alleviate growth-induced solid stress in the tumor.[64] By resisting stretching, the collagen fibers confine the proliferating cells and contribute to solid stress, which in turn increases interstitial fluid pressure and diminished blood flow. The depletion of collagen by collagenase alleviates interfibrillar stress, relaxes cancer cells, and stretches fibroblasts.[64] Likewise, the magnetically induced relaxation of peripheral collagen of the capsula as well as interior collagen has the potential to decompress blood and lymphatic vessels and to increase perfusion. Further studies are required to assess the consequences of nanoparticle-induced ECM modification on tumor elasticity, perfusion, and ultimately on neoplastic evolution in different models of human tumors. Apart from the established therapeutic potential of hyperthermia itself, spatially and temporally controlled nanoparticle heat generation could be proposed as an adjuvant pretreatment to briefly modulate the extracellular matrix in order to improve the delivery and efficacy of therapeutic agents injected afterward. Considering the physiological turnover of the ECM, there might be a window of opportunities after hyperthermia in which the access of a drug or other nanovectors to the tumor core can be improved. Supporting this assumption, we have shown that intravenous administration of doxorubicin had a better efficiency in inhibiting tumor growth when associated with magnetic hyperthermia (Figure 1D). Such finding is consistent with a better diffusion of the drug into the tumor interstitium, which is modified by nanocube local heating. We also quantified the tumor penetration of fluorescent 30−50 nm nanoparticles (AngioSPARK750) injected intravenously and found that AMF exposure for 3 × 30 min significantly increases the nanoparticle access to the tumor in comparison to nonexposed tumors (whole tumor fluorescence signal of 13.8 ± 4.3 *versus* 5.2 ± 0.8 in nonexposed tumors, Figure S11). Such strategy, using magnetic nanocubes as adjuvants to make the tumor microenvironment more favorable for other anticancer drugs and induce synergistic effects of a combined treatment, may be relevant for future therapies and is currently evaluated by our group.

CONCLUSION

In conclusion, we have shown that heat-generating PEG-coated iron oxide nanocubes interfere with the tumor extracellular matrix and have the potential to destructure the matrix under magnetic stimuli. This results in nanoparticle redistribution in the tumor during the three-cycle heating procedure, which also leads to the diminution of tumor growth. Nanocube-induced matrix destructuration also improves the tumor penetration of doxorubicin or nanoparticles injected intravenously and potentiate chemotherapy. Here we show that the local environment of nanocubes in tumors governs cubes' fate, magnetic behavior, and the therapeutic outcome of hyperthermia. Continued studies taking advantage of the

interactions between activatable nanoparticles and the tumor microenvironment are expected to reveal new clues to improve the effectiveness of cancer therapy.

MATERIALS AND METHODS

Synthesis of 19 nm Iron Oxide Nanocubes. The evolution of the SLP as a function of size prompted us to choose the 19 nm cubes, which show the best compromise between colloidal stability and optimized SLP. Water-soluble 19 nm iron oxide nanocubes of magnetite were prepared according to the protocol detailed in Guardia *et al.*[6] Briefly, 1 mmol of iron(III) acetylacetonate and 4 mmol of decanoic acid were mixed in 25 mL of dibenzyl ether. After degassing at room temperature for 45 min at 60 °C, the solution was heated to 200 °C (5 °C/min) under a nitrogen blanket and kept at this temperature for 2.5 h. Finally, the temperature was increased to reflux temperature (at a rate of 10 °C/min) and kept at this value for 1 h. After cooling to room temperature, the particles were collected by adding a 4-fold volume of acetone/chloroform and centrifuged at 8000 rpm for 10 min. The cubes were washed three times and dispersed in 15 mL of chloroform.

To coat the as-synthesized nanocubes with a stable PEG shell, PEG(3000)−gallol molecules were synthesized and exchanged at the nanoparticle surface as previously described.[17] Briefly, iron oxide nanocubes (10 mL, 1 g/L in Fe in $CHCl_3$) in chloroform were mixed with a PEG−gallol solution (20 mL, 0.05 M in $CHCl_3$) together with triethylamine (2 mL), and the mixture was diluted with 70 mL of toluene. After addition of 500 mL of Milli-Q water, the two phases were allowed to emulsify by gentle shaking. Acetone (100 mL) was added in order to destabilize the particles in the organic phase, and the mixture was shaken again gently up to emulsification. After phase separation, the aqueous phase was collected. This step was repeated three times. For purification, the aqueous solution containing the PEG−gallol-coated nanocubes was diluted with Milli-Q water and reconcentrated in centrifuge filters (MWCO 100 kDa, 3000 rpm). This step was repeated at least five times.

***In Vivo* Studies.** The experiments were performed in agreement with institutional animal use and care regulation of the Paris Cardiovascular Research Center animal facility. The animals were allowed to acclimate to this facility for at least 1 week before being used in the experiments and were fed a standard diet *ad libitum* throughout the experiments. *Studies on tumor bearing mice.* A total of 70 pathogen-free 8 week old female immunodeficient athymic nude NMRI mice, with the mean weight 20 ± 2 g, were used in the study (Janvier, France). Each mouse was subcutaneously injected in the left and right flank with 1.5×10^6 A431 human epidermoid carcinoma cells that were grown as adherent cells in complete RPMI culture medium and were resuspended in a volume of 100 μL physiological saline per inoculum. When the tumors reached approximately 40 mm^3 (measured with a caliper and calculated from the formula $V = Dd^2/2$, where D is the longest diameter, and d is the diameter perpendicular to D), the animals were divided in six groups. The animals of the group $G_{3\times HT}$ (N = 20) were injected in one of the tumors with a 50 μL volume of a sterile nanocube suspension corresponding to an iron concentration of 250 mM suspended in physiological saline medium. During the injection procedure, the tumor was immobilized with surgical tweezers and the suspension was injected in the tumor core at an injection rate of 10 μL/s while the animal was anesthetized with a ketamine/xylazine anesthesia. Ten minutes after nanocube injection and in the next two following days, the animals were exposed to the AMF under ketamine/xylazine anesthesia for 30 min per day. The animals of the group G_{Doxo} (N = 6) were injected with doxorubicin in the retro-orbital vein at a dose of 6 mg doxorubicin/kg of body weight. The animals of the group $G_{Doxo+3\times HT}$ (N = 6) were injected intravenously with doxorubicin and intratumorally with nanocubes and submitted to AMF 30 min exposure for three consecutive days as described above. The group $G_{control}$ (N = 20) consisted of tumor bearing animals that were injected neither with nanocubes nor with doxorubicin. A subpopulation of this control group (N = 7) was also submitted to ketamine/xylazine anesthesia and AMF exposure for 30 min per day for three consecutive days, but no significant difference was found in this subset and all the control tumors were pooled. Tumor growth was assessed every 2 days after injection of tumor cells. Ten to 12 days after nanocube injection, the volumes of control tumors were above the ethical limit and the mice were sacrificed. Tumor, liver, and spleen were excised and prepared for histology, TEM, magnetic measurements, and electron spin resonance. The animals of the fifth group, $G_{kinetics}$ (N = 10), were dedicated to a kinetic study, used to assess the early distribution of nanocubes within the tumor, with or without AMF exposure. The mice of this group were injected with the nanocube suspension into both tumors and were sacrificed at different time points (15 min, 6 h, 24 h, or 48 h after suspension administration; time points and numbers of tumors are summarized in supplementary Table 1). Tumors, livers, and spleens were excised and prepared for histology, TEM analysis, and magnetic measurements. The animals of the sixth group (N = 8) received an intravenous injection of AngioSPARK750 (PerkinElmer, 100 μL per mouse) and intratumoral injection of nanocubes. Half of the mice were exposed to the AMF exposure for 90 min under ketamine/xylazine anesthesia and the other half to the anesthesia alone. Tumors were harvested 2 h after the procedure and AngioSPARK750 fluorescence within whole tumors was imaged on a PhotonImager Optima imaging system (Biospace). *Long-term degradation studies on healthy mice.* For the complementary study of nanoparticles magnetic properties in liver and spleen and nanocube biodegradation, 26 mice were used. Group G_{Deg} consisted of 14 pathogen-free healthy female 8 week old C57/Bl6 mice (mean weight 20.5 ± 1 g) (Janvier, France), which were injected in the retro-orbital vein with sterile nanocubes suspended in 100 μL of physiological saline medium at a dose of 50 μmol/kg (injected dose of 56 μg iron). Twelve C57-Bl5 mice served as noninjected control ($G_{Deg\text{-}control}$). Three nanocube-injected mice and two control mice were sacrificed at each time point after nanoparticle injection (at days D1, D7, D14, D30, and D120, respectively). Livers and spleens were excised and prepared for TEM, histology, and ESR.

Magnetic Hyperthermia and Temperature Monitoring. The alternating magnetic field was generated by a MagneTerm AC system (Nanotherics, Corp.). AMF exposure was carried below the biologically safe limit using a magnetic field strength of 23.8 kA/m and a frequency of 111 kHz. A fluoro-optic thermometer fiber probe (Luxtron Corp., CA) was used to probe the temperature in the aqueous suspension of nanocubes and to monitor rectal temperature of treated mice. The mapping of the mouse skin surface temperature was monitored using a FLIR SC7000 infrared camera. All the acquisitions were processed by Altair software (FLIR Systems, Inc.).

MRI. Magnetic resonance imaging was performed on a Biospec 47/40 USR (40 cm bore actively shielded 4.7 T magnet) scanner interfaced to ParaVision software (both provided from Bruker Biospin GmbH, Rheinstetten, Germany). The whole body imaging protocol was performed with a volume transmission/reception RF coil for mice (Bruker), using a gradient echo sequence (TR/TE = 300/3 ms, flip angle = 30°, FOV = 3 cm, 8 averages and a pixel resolution of 117 × 117 μm) with slices (thickness = 1 mm) positioned over the liver, spleen, kidneys, and tumors (in tumor-bearing mice). Two mice per group (tumor bearing mice: G_{3XHT}, G_{noHT}, $G_{control}$) underwent MRI at D6 after nanocube injection, or at D1, D7, D14, D30, and D120 (mice from the degradation study: G_{Deg}, $G_{Deg\text{-}control}$). During the protocol, the animals were anesthetized with a 2% isofluorane (Aerrane, Baxter, Maurepas, France) supplied in air mixture, while their body temperature was kept constant by circulating

thermostated warm water. Image processing and analysis were made with the open source software OsiriX (3.9.2. version).

Histology. After excision, pieces of liver, spleen, lung, kidney, and tumor were fixed with pH 7.4 phosphate-buffered 10% formalin and processed by embedding in paraffin. Six micrometer thick sections were evaluated after hematoxylin and eosin, Masson's trichrome, or Pearls and Nuclear Fast Red staining (all from Sigma-Aldrich, Steinheim, Germany).

Transmission Electron Microscopy. Organs were cut into 1 mm^3 pieces after excision and fixed with 2% glutaraldehyde in 0.1 M sodium cacodylate buffer, postfixed with 1% osmium tetroxide containing 1.5% potassium cyanoferrate, gradually dehydrated in ethanol, and embedded in Epon. Thin sections (70 nm) of selected zones were observed with Zeiss EM902 electron microscope operated at 80 keV.

Magnetic Measurements and Electron Spin Resonance Quantification. Magnetization measurements were carried out on a vibrating sample magnetometer (PPMS, Quantum Design, Inc.) on fresh tumor, spleen, and liver samples and on colloidal suspension of iron oxide nanocubes. Field-dependent magnetization curves were measured at 310 K as a function of the external magnetic field in the range between 0 and 3×10^4 Gauss, and hysteresis curves were recorded for magnetic fields between −500 and +500 G. Temperature-dependent magnetization at a magnetic field of 50 G was recorded in the 5−310 K temperature range for zero-field-cooled and field-cooled sample (freezing field of 50 G). ESR spectrum were acquired at room temperature, using a Varian E102 EPR spectrometer operating at 9.25 GHz (microwave power 1 mW, modulation field 10G). ESR absorption signal of a known mass of the dried organs was obtained by double integration of the resonance spectrum. The calibration curve of the ESR signal was realized using various concentration of aqueous suspension of nanocubes (2 μL samples inserted in a glass capillary) as described before.[65]

Measurement of Collagen Interfibrillar Distance. Morphometric analysis has been performed on six different tumors (two per group, corresponding to HT-treated, injected only, and control tumors), where 100−300 fibrils were analyzed for each group. Transmission electron micrographs of collagen-rich zones were analyzed by ImageJ software (NIH, Bethesda, MD, USA). At first, the scale bar was set, then lines or squares were drawn perpendicular to the fringes of collagen fibers and the "Plot profile" function was used to obtain a two-dimensional graph of gray scale intensities of pixels along the selected zone. The comparison of gray scale intensities was used in order to avoid different contrast amplitudes in the micrographs. Consequently, we have chosen to define a threshold based on the amplitude of the gray variation (a threshold of x meaning min + x% × (max-min)), which was systematically applied to every image. The values of the x- and y-axes were then exported to Microsoft Excel, where the maxima of the curve, exceeding the 60% of the gray scale difference, were counted in the selected interval (generally between 500 nm and 2 μm). The 60% threshold was chosen because the number of peaks counted automatically had the best correlation with the manually counted fibers ($n_{auto} = n_{manual} \pm 1$; $N = 26$).

Statistics. Data are presented as standard deviation from the mean or as standard error of the mean. The statistical significance of the differences between groups was assessed with the Mann−Whitney U Test. Data were analyzed with Prism 3.0 version of GraphPad software (USA). A minimum of 95% confidence level was considered significant.

Conflict of Interest: The authors declare no competing financial interest.

Acknowledgment. This work was supported by the European project Magnifyco (Contract NMP4-SL-2009-228622) and ENCITE (J.K.-T.) (European Network for Cell Imaging and Tracking Expertise, Grant Agreement No. 201842) and by the Italian FIRB projects (Nanostructured oxides, Contract No. 588 BAP115AYN). We are grateful to S. Canevari for providing the tumor cells and for fruitful discussion, to J. Servais for hyperthermia setup, to the anatomopathology platform of the Georges Pompidou Hospital (Paris) for Masson trichrome staining, to L. Pidial and the personnel of the Paris Cardiovascular Research Center (PARCC) animal facility for their help in animal studies, G. Autret and S. Kusmia for MRI experiments (Small Animal Imaging Platform of PARCC, HEGP, Université Paris Descartes), C. Longin, S. Chat, M. Letheule and the platform MIMA2 at Inra of Jouy en Josas for TEM preparation, to M.F. Bureau and J. Seguin for help in optical imaging, to S. Nitti and G. Pugliese for helping with sample preparation, F. Gendron and the platform MPBT for magnetic measurements, J. Tabi for help in measurements of collagen fibers spacing, and J.C. Bacri and C. Le Visage for fruitful discussion.

Supporting Information Available: Figures S1−S11 and Tables S1 and S2. This material is available free of charge *via* the Internet at http://pubs.acs.org.

REFERENCES AND NOTES

1. Ferrari, M. Cancer Nanotechnology: Opportunities and Challenges. *Nat. Rev. Cancer* **2005**, *5*, 161–171.
2. Pernia Leal, M.; Torti, A.; Riedinger, A.; La Fleur, R.; Petti, D.; Cingolani, R.; Bertacco, R.; Pellegrino, T. Controlled Release of Doxorubicin Loaded within Magnetic Thermo-Responsive Nanocarriers under Magnetic and Thermal Actuation in a Microfluidic Channel. *ACS Nano* **2012**, *6*, 10535–10545.
3. Brulé, S.; Levy, M.; Wilhelm, C.; Letourneur, D.; Gazeau, F.; Ménager, C.; Le Visage, C. Doxorubicin Release Triggered by Alginate Embedded Magnetic Nanoheaters: A Combined Therapy. *Adv. Mater.* **2011**, *23*, 787–790.
4. Yoo, D.; Lee, J.-H.; Shin, T.-H.; Cheon, J. Theranostic Magnetic Nanoparticles. *Acc. Chem. Res.* **2011**, *44*, 863–874.
5. Lee, J.-H.; Jang, J.-t.; Choi, J.-s.; Moon, S. H.; Noh, S.-h.; Kim, J.-w.; Kim, J.-G.; Kim, I.-S.; Park, K. I.; Cheon, J. Exchange-Coupled Magnetic Nanoparticles for Efficient Heat Induction. *Nat. Nanotechnol.* **2011**, *6*, 418–422.
6. Guardia, P.; Di Corato, R.; Lartigue, L.; Wilhelm, C.; Espinosa, A.; Garcia-Hernandez, M.; Gazeau, F.; Manna, L.; Pellegrino, T. Water-Soluble Iron Oxide Nanocubes with High Values of Specific Absorption Rate for Cancer Cell Hyperthermia Treatment. *ACS Nano* **2012**, *6*, 3080–3091.
7. Bae, K. H.; Park, M.; Do, M. J.; Lee, N.; Ryu, J. H.; Kim, G. W.; Kim, C.; Park, T. G.; Hyeon, T. Chitosan Oligosaccharide-Stabilized Ferrimagnetic Iron Oxide Nanocubes for Magnetically Modulated Cancer Hyperthermia. *ACS Nano* **2012**, *6*, 5266–5273.
8. Lartigue, L.; Hugounenq, P.; Alloyeau, D.; Clarke, S. P.; Lévy, M.; Bacri, J.-C.; Bazzi, R.; Brougham, D. F.; Wilhelm, C.; Gazeau, F. Cooperative Organization in Iron Oxide Multi-Core Nanoparticles Potentiates Their Efficiency as Heating Mediators and MRI Contrast Agents. *ACS Nano* **2012**, *6*, 10935–10949.
9. van Landeghem, F. K.; Maier-Hauff, K.; Jordan, A.; Hoffmann, K.-T.; Gneveckow, U.; Scholz, R.; Thiesen, B.; Brück, W.; von Deimling, A. Post-Mortem Studies in Glioblastoma Patients Treated with Thermotherapy Using Magnetic Nanoparticles. *Biomaterials* **2009**, *30*, 52–57.
10. Silva, A. C.; Oliveira, T. R.; Mamani, J. B.; Malheiros, S. M.; Malavolta, L.; Pavon, L. F.; Sibov, T. T.; Amaro, E., Jr.; Tannús, A.; Vidoto, E. L. Application of Hyperthermia Induced by Superparamagnetic Iron Oxide Nanoparticles in Glioma Treatment. *Int. J. Nanomed.* **2011**, *6*, 591–603.
11. Johannsen, M.; Thiesen, B.; Wust, P.; Jordan, A. Magnetic Nanoparticle Hyperthermia for Prostate Cancer. *Int. J. Hyperthermia* **2010**, *26*, 790–795.
12. Issels, R. D.; Lindner, L. H.; Verweij, J.; Wust, P.; Reichardt, P.; Schem, B.-C.; Abdel-Rahman, S.; Daugaard, S.; Salat, C.; Wendtner, C.-M. Neo-Adjuvant Chemotherapy Alone or with Regional Hyperthermia for Localised High-Risk Soft-Tissue Sarcoma: A Randomised Phase 3 Multicentre Study. *Lancet Oncol.* **2010**, *11*, 561–570.
13. Maier-Hauff, K.; Ulrich, F.; Nestler, D.; Niehoff, H.; Wust, P.; Thiesen, B.; Orawa, H.; Budach, V.; Jordan, A. Efficacy and Safety of Intratumoral Thermotherapy Using Magnetic Iron-Oxide Nanoparticles Combined with External Beam Radiotherapy on Patients with Recurrent Glioblastoma Multiforme. *J. Neurooncol.* **2011**, *103*, 317–324.

14. Van der Zee, J.; González, D.; van Rhoon, G. C.; van Dijk, J. D.; van Putten, W. L.; Hart, A. A. Comparison of Radiotherapy Alone with Radiotherapy Plus Hyperthermia in Locally Advanced Pelvic Tumours: A Prospective, Randomised, Multicentre Trial. *Lancet* **2000**, *355*, 1119–1125.
15. Wust, P.; Hildebrandt, B.; Sreenivasa, G.; Rau, B.; Gellermann, J.; Riess, H.; Felix, R.; Schlag, P. Hyperthermia in Combined Treatment of Cancer. *Lancet Oncol.* **2002**, *3*, 487–497.
16. Noh, S.-h.; Na, W.; Jang, J.-t.; Lee, J.-H.; Lee, E. J.; Moon, S. H.; Lim, Y.; Shin, J.-S.; Cheon, J. Nanoscale Magnetism Control *via* Surface and Exchange Anisotropy for Optimized Ferrimagnetic Hysteresis. *Nano Lett.* **2012**, *12*, 3716–3721.
17. Lartigue, L.; Alloyeau, D.; Kolosnjaj-Tabi, J.; Javed, Y.; Guardia, P.; Riedinger, A.; Péchoux, C.; Pellegrino, T.; Wilhelm, C.; Gazeau, F. Biodegradation of Iron Oxide Nanocubes: High-Resolution *In Situ* Monitoring. *ACS Nano* **2013**, *7*, 3939–3952.
18. Jain, R. K.; Stylianopoulos, T. Delivering Nanomedicine to Solid Tumors. *Nat. Rev. Clin. Oncol.* **2010**, *7*, 653–664.
19. Torosean, S.; Flynn, B.; Axelsson, J.; Gunn, J.; Samkoe, K. S.; Hasan, T.; Doyley, M. M.; Pogue, B. W. Nanoparticle Uptake in Tumors Is Mediated by the Interplay of Vascular and Collagen Density with Interstitial Pressure. *Nanomed. Nanotechnol.* **2012**, *9*, 151–158.
20. Cichon, M. A.; Degnim, A. C.; Visscher, D. W.; Radisky, D. C. Microenvironmental Influences That Drive Progression from Benign Breast Disease to Invasive Breast Cancer. *J. Mammary Gland Biol. Neoplasia* **2010**, *15*, 389–397.
21. Cirri, P.; Chiarugi, P. Cancer Associated Fibroblasts: The Dark Side of the Coin. *Am. J. Cancer Res.* **2011**, *1*, 482–497.
22. Nerenberg, P. S.; Salsas-Escat, R.; Stultz, C. M. Collagen: A Necessary Accomplice in the Metastatic Process. *Cancer Genomics Proteomics* **2007**, *4*, 319–327.
23. van Kempen, L. C.; Ruiter, D. J.; van Muijen, G. N.; Coussens, L. M. The Tumor Microenvironment: A Critical Determinant of Neoplastic Evolution. *Eur. J. Cell Biol.* **2003**, *82*, 539–548.
24. Ji, T.; Zhao, Y.; Ding, Y.; Nie, G. Using Functional Nanomaterials To Target and Regulate the Tumor Microenvironment: Diagnostic and Therapeutic Applications. *Adv. Mater.* **2013**, *25*, 3508–3525.
25. Sounni, N. E.; Noel, A. Targeting the Tumor Microenvironment for Cancer Therapy. *Clin. Chem.* **2013**, *59*, 85–93.
26. Perrault, S. D.; Walkey, C.; Jennings, T.; Fischer, H. C.; Chan, W. C. W. Mediating Tumor Targeting Efficiency of Nanoparticles through Design. *Nano Lett.* **2009**, *9*, 1909–1915.
27. Chauhan, V. P.; Popović, Z.; Chen, O.; Cui, J.; Fukumura, D.; Bawendi, M. G.; Jain, R. K. Fluorescent Nanorods and Nanospheres for Real-Time *In Vivo* Probing of Nanoparticle Shape-Dependent Tumor Penetration. *Angew. Chem., Int. Ed.* **2011**, *50*, 11417–11420.
28. Han, H.-S.; Martin, J. D.; Lee, J.; Harris, D. K.; Fukumura, D.; Jain, R. K.; Bawendi, M. Spatial Charge Configuration Regulates Nanoparticle Transport and Binding Behavior *in Vivo*. *Angew. Chem., Int. Ed.* **2013**, *52*, 1414–1419.
29. Minchinton, A. I.; Tannock, I. F. Drug Penetration in Solid Tumours. *Nat. Rev. Cancer* **2006**, *6*, 583–592.
30. Ding, Y.; Li, S.; Nie, G. Nanotechnological Strategies for Therapeutic Targeting of Tumor Vasculature. *Nanomedicine* **2013**, *8*, 1209–1222.
31. Perrault, S. D.; Chan, W. C. W. *In Vivo* Assembly of Nanoparticle Components To Improve Targeted Cancer Imaging. *Proc. Natl. Acad. Sci. U.S.A.* **2010**, *107*, 11194–11199.
32. Wong, C.; Stylianopoulos, T.; Cui, J.; Martin, J.; Chauhan, V. P.; Jiang, W.; Popović, Z.; Jain, R. K.; Bawendi, M. G.; Fukumura, D. Multistage Nanoparticle Delivery System for Deep Penetration into Tumor Tissue. *Proc. Natl. Acad. Sci. U.S.A.* **2011**, *108*, 2426–2431.
33. Sano, K.; Nakajima, T.; Choyke, P. L.; Kobayashi, H. Markedly Enhanced Permeability and Retention Effects Induced by Photo-immunotherapy of Tumors. *ACS Nano* **2012**, *7*, 717–724.
34. Ramanujan, S. Diffusion and Convection in Collagen Gels: Implications for Transport in the Tumor Interstitium. *Biophys. J.* **2002**, *83*, 1650–1660.
35. Fortin, J. P.; Gazeau, F.; Wilhelm, C. Intracellular Heating of Living Cells through Neel Relaxation of Magnetic Nanoparticles. *Eur. Biophys. J.* **2008**, *37*, 223–228.
36. Mamiya, H.; Jeyadevan, B. Hyperthermic Effects of Dissipative Structures of Magnetic Nanoparticles in Large Alternating Magnetic Fields. *Sci. Rep.* **2011**, *1*, 1–7.
37. Serantes, D.; Baldomir, D.; Martinez-Boubeta, C.; Simeonidis, K.; Angelakeris, M.; Natividad, E.; Castro, M.; Mediano, A.; Chen, D.-X.; Sanchez, A.; *et al.* Influence of Dipolar Interactions on Hyperthermia Properties of Ferromagnetic Particles. *J. Appl. Phys.* **2010**, *108*, 073911–073915.
38. Attaluri, A.; Ma, R.; Qiu, Y.; Li, W.; Zhu, L. Nanoparticle Distribution and Temperature Elevations in Prostatic Tumours in Mice during Magnetic Nanoparticle Hyperthermia. *Int. J. Hyperthermia* **2011**, *27*, 491–502.
39. Dutz, S.; Kettering, M.; Hilger, I.; Müller, R.; Zeisberger, M. Magnetic Multicore Nanoparticles for Hyperthermia—Influence of Particle Immobilization in Tumour Tissue on Magnetic Properties. *Nanotechnology* **2011**, *22*, 265102–265107.
40. Alphandéry, E.; Faure, S. P.; Seksek, O.; Guyot, F. O.; Chebbi, I. N. Chains of Magnetosomes Extracted from Amb-1 Magnetotactic Bacteria for Application in Alternative Magnetic Field Cancer Therapy. *ACS Nano* **2011**, *5*, 6279–6296.
41. Hergt, R.; Dutz, S. Magnetic Particle Hyperthermia—Biophysical Limitations of a Visionary Tumour Therapy. *J. Magn. Magn. Mater.* **2007**, *311*, 187–192.
42. Levy, M.; Luciani, N.; Alloyeau, D.; Elgrabli, D.; Deveaux, V.; Pechoux, C.; Chat, S.; Wang, G.; Vats, N.; Gendron, F.; *et al.* Long Term *In Vivo* Biotransformation of Iron Oxide Nanoparticles. *Biomaterials* **2011**, *32*, 3988–3999.
43. Levy, M.; Gazeau, F.; Bacri, J. C.; Wilhelm, C.; Devaud, M. Modeling Magnetic Nanoparticle Dipole−Dipole Interactions inside Living Cells. *Phys. Rev. B* **2011**, *84*, 075480–070754.
44. Pennes, H. H. Analysis of Tissue and Arterial Blood Temperatures in the Resting Human Forearm. *J. Appl. Physiol.* **1998**, *85*, 5–34.
45. Cervadoro, A.; Giverso, C.; Pande, R.; SaSrangi, S.; Preziosi, L.; Wosik, J.; Brazdeikis, A.; Decuzzi, P. Design Maps for the Hyperthermic Treatment of Tumors with Superparamagnetic Nanoparticles. *PLoS One* **2013**, *8*, e57332.
46. Mu, C.; Li, D.; Lin, W.; Ding, Y.; Zhang, G. Temperature Induced Denaturation of Collagen in Acidic Solution. *Biopolymers* **2007**, *86*, 282–287.
47. Liu, Y.; Liu, L.; Chen, M.; Zhang, Q. Double Thermal Transitions of Type I Collagen in Acidic Solution. *J. Biomol. Struct. Dyn.* **2013**, *31*, 862–873.
48. Stylianopoulos, T.; Diop-Frimpong, B.; Munn, L. L.; Jain, R. K. Diffusion Anisotropy in Collagen Gels and Tumors: The Effect of Fiber Network Orientation. *Biophys. J.* **2010**, *99*, 3119–3128.
49. Diop-Frimpong, B.; Chauhan, V. P.; Krane, S.; Boucher, Y.; Jain, R. K. Losartan Inhibits Collagen I Synthesis and Improves the Distribution and Efficacy of Nanotherapeutics in Tumors. *Proc. Natl. Acad. Sci. U.S.A.* **2011**, *108*, 2909–2914.
50. Alexandrakis, G.; Brown, E. B.; Tong, R. T.; McKee, T. D.; Campbell, R. B.; Boucher, Y.; Jain, R. K. Two-Photon Fluorescence Correlation Microscopy Reveals the Two-Phase Nature of Transport in Tumors. *Nat. Med.* **2004**, *10*, 203–207.
51. Giustini, A.; Ivkov, R.; Hoopes, P. Magnetic Nanoparticle Biodistribution Following Intratumoral Administration. *Nanotechnology* **2011**, *22*, 345101–345107.
52. Jordan, A.; Scholz, R.; Wust, P.; Fähling, H.; Felix, R. Magnetic Fluid Hyperthermia (MFH): Cancer Treatment with AC Magnetic Field Induced Excitation of Biocompatible Superparamagnetic Nanoparticles. *J. Magn. Magn. Mater.* **1999**, *201*, 413–419.
53. Jordan, A.; Scholz, R.; Wust, P.; Fahling, H.; Krause, J.; Wlodarczyk, W.; Sander, B.; Vogl, T.; Felix, R. Effects of Magnetic Fluid Hyperthermia (MFH) on C3h Mammary Carcinoma *in Vivo*. *Int. J. Hyperthermia* **1997**, *13*, 587–605.

54. Gerweck, L. E.; Vijayappa, S.; Kozin, S. Tumor Ph Controls the *In Vivo* Efficacy of Weak Acid and Base Chemotherapeutics. *Mol. Cancer Ther.* **2006**, *5*, 1275–1279.
55. Persikov, A. V.; Xu, Y.; Brodsky, B. Equilibrium Thermal Transitions of Collagen Model Peptides. *Protein Sci.* **2004**, *13*, 893–902.
56. Xu, Y. Thermal Stability of Collagen Triple Helix. *Methods Enzymol.* **2009**, *466*, 211–232.
57. Song, C. W.; Lyons, L. C.; Griffin, R. J.; Makepeace, C. M. Thermosensitization by Lowering Intracellular pH with 5-(*N*-Ethyl-*N*-isopropyl) Amiloride. *Radiother. Oncol.* **1993**, *27*, 252–258.
58. Thistlethwaite, A. J.; Leeper, D. B.; Moylan, D. J., III; Nerlinger, R. E. pH Distribution in Human Tumors. *Int. J. Radiat. Oncol., Biol., Phys.* **1985**, *11*, 1647–1652.
59. Horgan, D. J.; Kurth, L. B.; Kuypers, R. pH Effect on Thermal Transition Temperature of Collagen. *J. Food Sci.* **1991**, *56*, 1203–1204.
60. McKee, T. D.; Grandi, P.; Mok, W.; Alexandrakis, G.; Insin, N.; Zimmer, J. P.; Bawendi, M. G.; Boucher, Y.; Breakefield, X. O.; Jain, R. K. Degradation of Fibrillar Collagen in a Human Melanoma Xenograft Improves the Efficacy of an Oncolytic Herpes Simplex Virus Vector. *Cancer Res.* **2006**, *66*, 2509–2513.
61. Mok, W.; Boucher, Y.; Jain, R. K. Matrix Metalloproteinases-1 and -8 Improve the Distribution and Efficacy of an Oncolytic Virus. *Cancer Res.* **2007**, *67*, 10664–10668.
62. Hong, C. S.; Fellows, W.; Niranjan, A.; Alber, S.; Watkins, S.; Cohen, J. B.; Glorioso, J. C.; Grandi, P. Ectopic Matrix Metalloproteinase-9 Expression in Human Brain Tumor Cells Enhances Oncolytic Hsv Vector Infection. *Gene Ther.* **2010**, *17*, 1200–1205.
63. Kanapathipillai, M.; Mammoto, A.; Mammoto, T.; Kang, J. H.; Jiang, E.; Ghosh, K.; Korin, N.; Gibbs, A.; Mannix, R.; Ingber, D. E. Inhibition of Mammary Tumor Growth Using Lysyl Oxidase-Targeting Nanoparticles To Modify Extracellular Matrix. *Nano Lett.* **2012**, *12*, 3213–3217.
64. Stylianopoulos, T.; Martin, J. D.; Chauhan, V. P.; Jain, S. R.; Diop-Frimpong, B.; Bardeesy, N.; Smith, B. L.; Ferrone, C. R.; Hornicek, F. J.; Boucher, Y.; *et al.* Causes, Consequences, and Remedies for Growth-Induced Solid Stress in Murine and Human Tumors. *Proc. Natl. Acad. Sci. U.S.A.* **2012**, *109*, 15101–15108.
65. Wilhelm, C.; Gazeau, F.; Bacri, J. C. Magnetophoresis and Ferromagnetic Resonance of Magnetically Labeled Cells. *Eur. Biophys. J.* **2002**, *31*, 118–125.